ADVANCED FUNCTIONAL MATERIALS
www.afm-journal.de

Hysteresis, Loss and Nonlinearity in Epitaxial $PbZr_{0.55}Ti_{0.45}O_3$ Films: A Polarization Rotation Model

Philip Lucke, Muharrem Bayraktar, Yorick A. Birkhölzer, Mohammadreza Nematollahi, Andrey Yakshin, Guus Rijnders, Fred Bijkerk, and Evert P. Houwman**

The phenomena of hysteresis, ferroelectric loss, and nonlinearity are investigated for the strain and polarization of a monoclinic, epitaxial $Pb(Zr,Ti)O_3$ film over the 70 Hz to 5 kHz frequency range at sub-coercive excitation fields and zero electrical bias. For the strain, a linear hysteretic behavior is found, whereas the polarization shows a strongly nonlinear hysteretic behavior. In contrast to polycrystalline structures (for instance in ceramics or chemical solution deposited thin films), the commonly referred Rayleigh model cannot explain the observed behavior. A new model is presented, based on the rotation of the polarization vector within the monoclinic or rhombohedral unit cell under an applied electric field, with the viscous interaction of domains accompanying the unit cell deformation. The model explains the amplitude and frequency scaling of the strain, polarization, and loss tangent as well as the observed higher harmonics of polarization in the measured epitaxial $Pb(Zr,Ti)O_3$ films. It is concluded that the nonlinear response and the hysteretic loss originate from two separate physical processes. The nonlinear response is attributed to the nonlinear angular rotation of the polarization vector, whereas the hysteresis and ferroelectric loss are due to a viscous interaction of domains while the polarization vector is rotating.

1. Introduction

Nowadays piezoelectric ceramics and thin films are widely applied in sensors, actuators, ferroelectric memories, and energy harvesters.[1–8] Especially $PbZr_xTi_{1-x}O_3$ (PZT) is commonly used because of its remarkable piezoelectric properties both in ceramics and thin films.[9–11] One of the challenges in the application of piezoelectric materials is the hysteresis that manifests itself, for example, as positioning inaccuracy of actuators and energy loss in energy harvesting applications.[12] Therefore, an accurate description and identification of the origin of hysteresis and energy loss in piezoelectric materials has always been an important topic.

Already early on, the interaction of domains was identified as a possible source of sub-coercive field hysteresis and associated with that dielectric and piezoelectric losses. The observed dielectric losses have been described by viscous motion of the domain walls (DWs) and in this way Arlt and Dederichs related the hysteretic piezoelectric response to the vibration of 90° DWs under an applied external oscillating field.[13–17] However, with this model it is not possible to explain the observed field amplitude dependence of the dielectric/piezoelectric loss. Damjanovic described the field amplitude dependent dielectric/piezoelectric loss behavior in PZT ceramics with an adaptation of the Rayleigh model that has often been used for the description of hysteresis in ferromagnets and later also in ferroelectrics.[18–21] Microscopically the nonlinear field response, of which hysteresis is considered to be a consequence, has been related to the stochastic interaction of DWs with defects, causing so-called Barkhausen jumps of the DWs from a local energy minimum to the next.[22,23] This model allows describing the effect of the amplitude and frequency of the applied electric field, to our best knowledge, only for polycrystalline ceramics and chemical solution deposited (CSD) thin films.[24–27] However we note that the Rayleigh model is based on a stochastic effect that does not take into account the crystal symmetry of the material. This works well for polycrystalline material, but one expects hysteresis and especially the nonlinearity to behave differently for different crystallinities, as the functional properties of materials with different crystal symmetries and crystal orientations, respond

P. Lucke, Dr. M. Bayraktar, Dr. M. Nematollahi,[+] Dr. A. Yakshin, Prof. F. Bijkerk
Industrial Focus Group XUV Optics
MESA+ Institute of Nanotechnology
University of Twente
Enschede, The Netherlands
E-mail: m.bayraktar@utwente.nl
Y. A. Birkhölzer, Prof. G. Rijnders, Dr. E. P. Houwman
Inorganic Material Science
MESA+ Institute of Nanotechnology
University of Twente
Enschede, The Netherlands
E-mail: e.p.houwman@utwente.nl
The ORCID identification number(s) for the author(s) of this article can be found under https://doi.org/10.1002/adfm.202005397.

[+]Present address: Trace Gas Research Group, Department of Molecular and Laser Physics, Institute of Molecules and Materials, Radboud University, Nijmegen, The Netherlands

DOI: 10.1002/adfm.202005397

differently to the applied electric field.[28] Epitaxial thin films are therefore excellent model systems to investigate the relation between crystal symmetry and hysteresis as they resemble the behavior of perfect single crystal systems with low levels of defects. In addition, such investigation may render practical benefits since many future high-performance applications are expected to be based on epitaxial films because of their better performance. To our knowledge there are no studies available on the frequency and amplitude dependency of hysteresis, loss, and nonlinearity in epitaxial PZT thin films.

We investigated the hysteresis, loss, and nonlinearity of poled, epitaxial, (001)-oriented, monoclinic PZT films at zero bias field for excitation electric field amplitudes up to half of the coercive field and in the frequency range of 70 Hz to 5 kHz. To explain the observed strain, polarization and dielectric/piezoelectric loss behavior, we propose a new model by considering the oscillatory rotation of the polarization vector in the monoclinic unit cell in response to an oscillating applied external electric field.

2. Model Development Using Experimental Constraints

Generally, hysteresis in ferro- and piezo-electric materials has been modeled with the Rayleigh model, which originates from the description of hysteresis in magnetic systems.[18–21] The Rayleigh model can be shown to be a limiting case of the Preisach model, which provides a statistical description of the transitions between local energy minima in an energy landscape under influence of an oscillatory field.[29–31] In the case of ferroelectrics, one assumes that DWs are locally trapped by defects and jump to new defect sites under the influence of the applied field, which is causing the hysteresis. In Section 1, Supporting Information, we summarize the Rayleigh model and several extensions of it, that have been suggested over time. The main features of these models are:

a) Nonlinear response and hysteresis are described by the same hysteresis parameter (generally denoted by α), therefore the magnitude of these phenomena are coupled.[21,24,25,32–38]
b) A Fourier decomposition of the hysteresis response only contains odd harmonics.[21,24,25,32–38] In one extension of the model, including 180° DW motion, an additional second harmonic arises, but no even order higher harmonics appear.[39–41]
c) The hysteresis loop is lenticularly shaped, which most clearly shows up in sharp endpoints of the loop. In some models a viscous loss term is added to the polarization response, reflecting viscous motion of the DWs under influence of the applied field. This viscous term introduces rounding of the hysteresis loop that becomes elliptically shaped. The viscous loss term may in some cases be the only reason for hysteresis.[32,42]
d) In the pure Rayleigh model the hysteresis loss does not contain an explicit frequency dependence, unless the dielectric or piezoelectric coefficient and/or the hysteresis parameters are implicitly frequency dependent.[26,27] In the models containing a viscous loss term, the loss scales linearly with frequency, apart from further implicit frequency dependencies.[32,42]
e) In the Rayleigh model the hysteresis loop is traversed counterclockwise (CCW), as one would expect for a lossy hysteresis process.

For the discussion here it is important to note that hysteresis models, as presented so far in literature, do not contain any relation with the crystal structure and crystal orientation of the materials to which the models are applied. These models may fairly well describe the hysteretic behavior of polycrystalline samples and probably also of many CSD derived thin films, however one would expect to see crystal symmetry dependence of the ferroelectric response in single crystals and epitaxial thin films.

The hysteresis measurements on our monoclinic, epitaxial PZT film show many deviations from the predictions of the Rayleigh model and its derivatives. Notably, we see only the fundamental harmonic in the strain response, whereas all even and odd harmonics up to the 5th order appear in the polarization response. Furthermore, the hysteresis loops have an elliptical shape and the loss tangent is found to scale linearly with frequency. For these reasons we conclude that none of the above-mentioned models can describe our measurement data and we propose a new model, based on the crystal symmetry, that describes the main observations.

2.1. Polarization Rotation Model

Here we describe a new model that can explain the observed hysteresis and nonlinearity in terms of the unit cell strain and polarization response induced by the applied electric field in (001)-oriented ferroelectric films with a rhombohedral or a monoclinic crystal symmetry or transitional states between these symmetries. The property we use here is that the (110)-plane is the symmetry plane in which the polarization vector rotates, that is, this plane contains the longest body diagonal of the unit cell such as in rhombohedral and monoclinic unit cells, or transitional states between these symmetries. **Figure 1**a shows one of the eight possible configurations of such a unit cell, as one would expect to be present in approximately equal fractions in an as-grown epitaxial thin film, organized in polarization domains, separated by DWs. The eight configurations correspond to unit cells with the polarization vector in one of the eight possible <111>-like directions. For fully relaxed rhombohedral unit cells these would be the <111> body diagonal directions. PZT films with top and bottom electrodes in the parallel plate configuration are considered to be poled in the downward direction (i.e., from top to bottom electrode) so that only the four configurations with the same downward oriented out-of-plane polarization component remain, which are organized in polarization domains separated by DWs. In this configuration, the polarization measurable across the film is,

$$P = P_S \cos(\theta) \tag{1}$$

where P_s is the spontaneous polarization and θ is the polarization angle between the [001]-axis and the polarization vector. For the PZT films that will be explored here, the reference spontaneous polarization value in bulk rhombohedral PZT(55/45) composition is P_s = 50 μC cm^{-2}.[43] For a fully

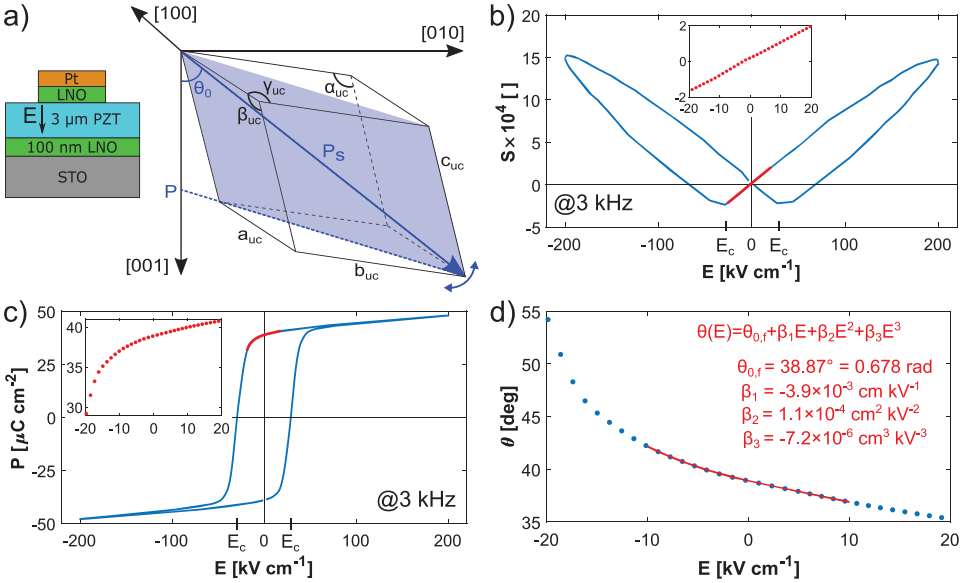

Figure 1. a) Schematic sample structure. Unstrained rhombohedral or monoclinic PZT unit cell with out-of-plane polarization component *P*. P_s is the spontaneous polarization vector length and θ_0 is the angle between the [001]-axis and the polarization vector. b) *S-E* and c) *P-E* loops for a large electric field amplitude, E_{max} = 200 kV cm^{-1} ≫ E_c. The insets show the magnified view of the –20 to 20 kV cm^{-1} sub-coercive field range of the falling branches. d) Field dependence of the polarization angle θ, calculated from the inset in (c). The red line gives the fit of a third order polynomial over the –10 to 10 kV cm^{-1} field range as explained in the text. All the measurements are at 3 kHz.

relaxed rhombohedral unit cell with the polarization vector in the body diagonal, θ equals θ_0 = 54.7° and hence P equals P_r = 29 µC cm^{-2}, the remanent polarization of the film.[43] In a film under compressive in-plane stress the polarization vector will rotate towards the out-of-plane direction so that the polarization angle of the film at zero field, $\theta_{0,f}$ decreases and the remanent polarization $P_{r,f}$ will increase. Under an applied electric field in the [001]-direction, the polarization vector rotates following the electric field. For downward oriented fields (i.e., positive voltage on the top electrode with respect to a grounded bottom electrode) the polarization vector will rotate towards the out-of-plane [001]-axis, decreasing θ, increasing P, and stretching the unit cell in [001]-direction by the piezoelectric effect. It is important to note that here, we only consider the oscillating electric field amplitudes below the coercive field value and assume that no polarization switching occurs. Additionally, we consider that the polarization extension is negligible in the considered sub-coercive electric field range.[44]

2.1.1. Strain Response

A typical strain-electric field (*S-E*) loop measured with a large electric field amplitude, far exceeding the coercive field, that is, the global *S-E* loop, is shown in Figure 1b. The measured strain is in good approximation linear (R^2 = 0.9987) with the applied field in the sub-coercive field range, as shown in the inset. In the first part of constructing a strain hysteresis model, we therefore take the strain to be linearly dependent and in-phase with the applied electric field $S_{ip}(t) = d_{33,f}\ E(t)$ in the sub-coercive field range that is explored in the hysteresis experiments. As we work with films, the piezoelectric properties of the films are reduced compared to bulk properties due to clamping by the substrate. Here $d_{33,f}$ is the effective piezoelectric coefficient in the out-of-plane direction of the clamped film. In Section 2, Supporting Information, we show that this linear dependence can be derived in good approximation from the Landau-Devonshire description of a single domain rhombohedral or monoclinic clamped film, at least for positive fields. An expression for $d_{33,f}$ for a clamped film in terms of elastic compliances and electrostrictive parameters, determined from the Landau-Devonshire model, is also given. The elliptic strain hysteresis loops observed in our experiments suggest that the piezoelectric loss is dominated by a viscous loss mechanism, for example due to DW motion as is commonly assumed for piezoelectric materials.[13,15,17] In the second part of the strain model, a viscous and out-of-phase term that is proportional to the time derivative of the in-phase part can be written as $S_{oop}(t) = \gamma_S\ \dot{S}_{ip}(t)$ in which γ_S is the viscosity coefficient. Total strain can be written as a summation of the in-phase and out-of-phase strain parts as $S(t) = S_{ip}(t) + S_{oop}(t)$. Hence, one arrives at a rather simple expression for the total strain response of the considered film to a small amplitude sinusoidal field, $E(t) = E_0 \sin(\omega t)$, from which the hysteresis properties can be determined

$$S(t) = d_{33,f}\ E(t) + \gamma_S d_{33,f} \dot{E}(t) = d_{33,f} E_0 \sin(\omega t) + \gamma_d \omega E_0 \cos(\omega t) \quad (2)$$

Here γ_d is the multiplication of the viscosity coefficient γ_S with the piezoelectric coefficient $d_{33,f}$. Because viscous processes cause a time lag of the unit cell expansion in response to increasing fields, one expects that $\gamma < 0$. Note that Equation (2) only describes the explicit excitation field amplitude and frequency dependence, but frequency dependent viscous interactions may lead to additional implicit frequency dependences of the parameters $d_{33,f}$ and γ_d. The nature of these viscous interactions is poorly understood and described in literature. We

do not include such interactions in our model, but extract these dependencies from frequency dependent measurements.

Equation (2) predicts a hysteretic strain that is linearly dependent on field amplitude. In the simplest case, that is, when $d_{33,f}$ and γ_d are independent of frequency, the hysteresis is linearly dependent on the frequency and amplitude. The maximum loop opening, $\Delta S_{open} = |S(\omega t = \pi) - S(\omega t = 0)| = |2\gamma_d \omega E_0|$ scales linearly with E_0 and is, if γ_d is not a function of frequency, also linearly with frequency. The strain loss, or the loss tangent, is obtained as the ratio of the viscous to non-viscous components of the strain:

$$\tan \delta_S = \left|\gamma_d \omega / d_{33,f}\right| = \left|\gamma_S \omega\right| \tag{3}$$

Interestingly, if $d_{33,f}$ and γ_d are independent of amplitude and frequency, the loss tangent is independent of the amplitude and scales linearly with the frequency, which will be verified in the results section. In comparison the Rayleigh model predicts a dependency of the loss tangent on the amplitude of the electric field, see Equation S1.8, Supporting Information, but on the other hand does not have an explicit frequency dependence.

2.1.2. Polarization Response

We assume that the polarization change is only due to polarization rotation and the effect of polarization vector extension is neglected.[45,46] For a positive field in the [001]-direction the polarization vector rotates towards the [001]-axis and for negative electric field towards the (001)-plane. The change of the polarization angle θ that is in-phase with the driving field can be described by $\theta_{ip}(E) = \theta_{0,f} + \Delta\theta(E)$, with $\theta_{0,f}$ the angle for a clamped film at zero field and $\Delta\theta(E)$ the small change of the angle with applied field. A typical global polarization-electric field (*P*-*E*) loop is shown in Figure 1c. The inset displays the part of the global loop in the field range –20 to 20 kV cm^{-1}. Here we only consider the decreasing field branch, as the film is poled downward. During small amplitude field cycling in the –10 to 10 kV cm^{-1} range, that is, well below the coercive-field so that no polarization switching occurs, the polarization tracks this branch back and forth.

Figure 1d gives the angle $\theta(E)$ calculated from the global *P*-*E* loop in Figure 1c using Equation (1). Fitting in the –10 to 10 kV cm^{-1} field range with a third order polynomial for $\Delta\theta(E) = \beta_1 E + \beta_2 E^2 + \beta_3 E^3$ in $\theta_{ip}(E)$ gives a very accurate description of the data ($R^2 = 0.9999$). We note that a third order polynomial is the lowest order polynomial that can accurately describe the asymmetry of the measured $\theta(E)$ data with respect to the y-axis. In the following we will see that the nonlinear $\Delta\theta(E)$ relation accounts for the nonlinear field amplitude dependence of the polarization hysteresis loops. In addition to this field dependence we assume a linear viscous interaction (again because the hysteresis loops have elliptic shapes for all frequencies and amplitudes) to be present in the polarization rotation model. Further on it is shown that this term will give rise to the hysteresis. Thus, we arrive at

$$\begin{aligned}\theta(E) &= \theta_{0,f} + \Delta\theta(E) + \gamma_P \Delta\dot{\theta}(E) \\ &= \theta_{0,f} + \beta_1 E + \beta_2 E^2 + \beta_3 E^3 + \gamma_P \dot{E}\left(\beta_1 + 2\beta_2 E + 3\beta_3 E^2\right)\end{aligned} \tag{4}$$

The magnitude, sign and required number of the β-coefficients are dependent on the strain state and consequently the substrate, the deposition temperature, the composition of the film, and the field range over which the angle fitting is performed.[47] As the angle should decrease with increasing field, we expect a priori that the non-viscous parameters β_1, $\beta_3 < 0$, and the viscous parameter $\gamma_P < 0$ because the response should lag behind the electric field, similar as for the strain response. The second order term β_2 gives rise to a possible asymmetry in the field sensitivity of $\Delta\theta(E)$. Since the magnitude of the viscous part is expected to be much smaller compared to non-viscous part, the angle-field dependence in Figure 1d has been fitted with Equation (4) excluding the viscous terms. The fit values are given in Figure 1d. It is seen that the expectations regarding the signs of the model parameters match the signs of the fitted values. In addition, the fit shows that $\beta_2 > 0$ and that $|\beta_1| > |\beta_2| > |\beta_3|$. The fitted $\theta_{0,f}$ value indicates that the zero field polarization vector is rotated by 15.9° from the rhombohedral body diagonal towards the [001]-axis. X-ray diffraction (XRD) analysis of the clamped PZT film, presented in the results section, shows that there is in-plane compressive strain of the unit cell, causing an out-of-plane tetragonal deformation of the cubic parent unit cell, leading to the observed rotation.

The dependence of the polarization to the angular change θ(E) can be rewritten as:

$$\begin{aligned}P(\theta) &= P_S \cos\left(\theta_{0,f} + \Delta\theta + \gamma_P \Delta\dot{\theta}\right) \\ &= P_{r,f}\left[\cos\left(\Delta\theta + \gamma_P \Delta\dot{\theta}\right) - \tan\left(\theta_{0,f}\right)\sin\left(\Delta\theta + \gamma_P \Delta\dot{\theta}\right)\right]\end{aligned} \tag{5}$$

where we have defined the remanent polarization of the clamped film as $P_{r,f} = P_S \cos(\theta_{0,f})$. As can be seen from Figure 1d $\Delta\theta(E)$ is of the order of a few degrees only, therefore we can use lowest order Taylor expansions of the sin and cos terms, resulting in a nonlinear, but analytically tractable polynomial expression for the time-dependent polarization response:

$$\begin{aligned}P(t) = P_{r,f}[&c_0 + c_{1,s}E_0 \sin(\omega t) + c_{1,c}E_0 \cos(\omega t) + c_{2,s}E_0^2 \sin(2\omega t) \\ &+ c_{2,c}E_0^2 \cos(2\omega t) + c_{3,s}E_0^3 \sin(3\omega t) + c_{3,c}E_0^3 \cos(3\omega t) \\ &+ c_{4,s}E_0^4 \sin(4\omega t) + c_{4,c}E_0^4 \cos(4\omega t) + c_{5,s}E_0^5 \sin(5\omega t) \\ &+ c_{5,c}E_0^5 \cos(5\omega t) + c_{6,s}E_0^6 \sin(6\omega t) + c_{6,c}E_0^6 \cos(6\omega t)]\end{aligned} \tag{6}$$

The *c*-coefficients are functions of the β-coefficients and E_0 which are given in Section 3, Supporting Information. Note that all coefficients are even functions of E_0. In addition, we give the values of the *c*-coefficients in the same section for E_0 = 10 kV cm^{-1} and f = 3 kHz, and show that the amplitude of the harmonics rapidly decreases with increasing harmonic number.

The Fourier expansion of Equation (6) shows that from the assumed $\theta(E)$ dependence one expects to measure in principle all even and odd order harmonics up to the 6th harmonic, with hysteresis being present in all harmonics. Higher order polynomial fitting and/or expansion gives rise to higher order hysteresis and even higher order harmonics, although with rapidly decreasing amplitudes.

The first and higher order hysteresis loops are centered around the point $P_{center} = P_{r,f} c_0(E_0, \omega) \approx P_{r,f}$. Within this model the amplitude of the *n*th harmonic is given by

$$\left|P_n\right| = P_{r,f}\left(E_0^n \sqrt{c_{n,s}^2 + c_{n,c}^2}\right) \tag{7}$$

The amplitude of the hysteresis loop is dominated by the amplitude of the first harmonic. The average slope of the loop is the effective dielectric constant (or the Rayleigh parameter $m(E_0)$ of Equation S1.2, Supporting Information), given in the polarization rotation model by $\varepsilon_{\text{eff}} \approx P_{r,f} c_{1,s}$

We will see that experimentally the harmonics are not sharp delta functions in the frequency domain as assumed in the model but show considerable frequency spreading. Consequently, the energy contained in the different harmonics, which is proportional to $P_n{}^2$, is redistributed and the measured harmonic amplitudes P_n at the harmonic frequencies $\omega_n = n\omega$ differ from the calculated values described by Equation S3.1 and S3.2, Supporting Information. However, the type of dependence on field amplitude and frequency is expected to be conserved.

As the magnitude of the harmonics is the easiest parameter that can be extracted from the measurement, we give the expected scaling of $|P_n|$ with the amplitude of the electric field, following Equation (7):

$$\begin{aligned}
|P_1| &= P_{r,f}\left(E_0\sqrt{c_{1,s}^2+c_{1,c}^2}\right) \approx P_{r,f}\left(k_{1,1}E_0 + k_{1,3}E_0^3\right)\\
|P_2| &= P_{r,f}\left(E_0^2\sqrt{c_{2,s}^2+c_{2,c}^2}\right) \approx P_{r,f}\left(k_{2,2}E_0^2 + k_{2,4}E_0^4\right)\\
|P_3| &= P_{r,f}\left(E_0^3\sqrt{c_{3,s}^2+c_{3,c}^2}\right) \approx P_{r,f}\left(k_{3,3}E_0^3 + k_{3,5}E_0^5\right)\\
|P_4| &= P_{r,f}\left(E_0^4\sqrt{c_{4,s}^2+c_{4,c}^2}\right) \approx P_{r,f}\left(k_{4,4}E_0^4 + k_{4,6}E_0^6\right)\\
|P_5| &= P_{r,f}\left(E_0^5\sqrt{c_{5,s}^2+c_{5,c}^2}\right) \approx P_{r,f}\left(k_{5,5}E_0^5\right)\\
|P_6| &= P_{r,f}\left(E_0^6\sqrt{c_{6,s}^2+c_{6,c}^2}\right) \approx P_{r,f}\left(k_{6,6}E_0^6\right)
\end{aligned} \tag{8}$$

The $k_{n,m}$ coefficients are functions of the β-coefficients and ω, where n is the order of the harmonic and m the power of the field amplitude. The exact expressions for the k-coefficients are given in Section 3, Supporting Information, however these are upper limits of the harmonic amplitude, since much energy is leaked away lowering the measured polarization amplitudes and causing the frequency spreading of the harmonics. Equation (8) predicts that the amplitude of the harmonics scale with an even or odd power polynomial of the field amplitude.

The loss tangent for the polarization can be written straightforwardly as the ratio of viscous to non-viscous part of the fundamental harmonic when the polarization signal is approximated by the fundamental harmonic as:

$$P \approx P_{r,f}\left[c_{1,s}E_0\sin(\omega t) + c_{1,c}E_0\cos(\omega t)\right] \tag{9}$$

The polarization loss tangent is then:

$$\tan\delta_P \approx \left|\frac{c_{1,c}}{c_{1,s}}\right| \approx \left|\frac{-\beta_1\gamma_P\omega\left[\left(\frac{3\beta_3\tan(\theta_{0,f})}{4\beta_1}+\frac{3\beta_2}{4}\right)E_0^2+\tan(\theta_{0,f})\right]}{-\beta_1\left[\left(\frac{3\beta_2}{4}+\frac{3\beta_3\tan(\theta_{0,f})}{4\beta_1}\right)E_0^2+\tan(\theta_{0,f})\right]}\right| = |\gamma_P\omega| \tag{10}$$

This is the same expression as for the loss in the strain hysteresis. The loss tangent should be amplitude independent and should be a linear function of the frequency. This observation will become important in the discussion of the measured amplitude dependence of the polarization loss tangent in the results section.

3. Results and Discussion

The polarization rotation model considers a rhombohedral or monoclinic unit cell and predicts the observed scaling of strain and polarization with driving field amplitude and frequency. First, we present and discuss the measurements on the crystal structure, showing that the investigated film is composed of compressively strained, monoclinic, polydomain PZT. Secondly, the data treatment procedure, which is required to obtain strain and polarization information from generally noisy and drifting raw measurement data, is presented. The film used in the experiments was a 3 µm thick PZT film, with 55/45 Zr/Ti ratio, sandwiched between $LaNiO_3$ (LNO) electrodes. All layers were grown subsequently by pulsed laser deposition (PLD) on a (001)-oriented $SrTiO_3$ (STO) substrate without breaking the vacuum. The strain and polarization were measured with a double beam laser interferometer (aixDBLI) combined with the aixACCT TF-2000 Analyzer. See the Experimental Section for more information about the experimental procedures. Finally, we present the analysis of the treated strain and polarization hysteresis measurement data in terms of the polarization rotation model.

3.1. Crystal Structure

XRD analysis was performed on the LNO/PZT/LNO heterostructure as explained in Section 4, Supporting Information. The data could be best fitted with a tetragonally deformed rhombohedral (from crystallographic point of view monoclinic) unit cell structure, with a four-fold in-plane symmetry, that is, the unit cells are rotated by integer multiples of 90° with respect to each other. The PZT in-plane unit-cell parameters are $a_{uc} = b_{uc} = 4.081$ Å, and the out-of-plane lattice parameter is $c_{uc} = 4.097$ Å. Here the subscript uc is used with unit-cell parameters a, b, and c to distinguish them from other parameters with the same symbols. The angle between the in-plane lattice vectors is obtained as $\gamma_{uc} \approx 89.79°$, while the angles between in-plane and out-of-plane are $\alpha_{uc} = \beta_{uc} \approx 89.74°$. The c-axis of all unit cells is perpendicular to the substrate, hence the (001)-planes are tilted by 0.26°. The unit cell volume is $V_{uc} \approx a_{uc}{}^2 c_{uc} = 68.27$ Å^3 and the pseudocubic lattice parameter is given by $a_{pc} = V_{pc}{}^{1/3} = 4.087$ Å. Because of the rhombohedral lattice symmetry, the polarization vector is expected to rotate in the (110)-plane of each unit cell.[48] The structure appears to have been pushed to the monoclinic side, which might be due to a high density of point defects, indicated by the slightly higher unit cell volume, and the clamping to the substrate, introducing strain. The small tetragonality ratio $c_{uc}/a_{uc} = 1.004$ is a consequence of the in-plane compressive strain, due to the difference in thermal expansion of the film and substrate, and is estimated as $\varepsilon_{ip} = (a_{uc} - a_{pc})/a_{pc} = -0.13\%$.[49] For films thicker than a few hundred nanometer, the substrate-induced strain is mainly due to the difference in thermal expansion coefficients between film and substrate, since at deposition

temperature the bulk of the film can be assumed to be fully relaxed from epitaxial strain due to the incorporation of (dislocation) defects. The room temperature strain, caused by the difference in thermal expansion coefficients (4.6 ppm K^{-1} for the PZT 55/45 film, which is obtained by interpolation of the data for PZT 60/40 and PZT 50/50 films, and 11.7 ppm K^{-1} for the STO substrate) when cooling down from deposition to room temperature and corrected for the volume increase due to the paraelectric-to-ferroelectric phase transition, is calculated as $S_m^0 \approx -0.003$.[45,46] This explains the compressive strain in the film deduced from the XRD measurements.

3.2. Measured Strain and Polarization Response

Figure 2 shows in the left and right column subfigures the raw data in time and frequency domains, of respectively the applied electric field $E = E_0 \sin(\omega t)$, the measured strain S, and the measured polarization P response, for a measurement frequency of $f = \omega/2\pi = 3$ kHz and electric field amplitude of $E_0 = 10$ kV cm^{-1}. Figure 2a shows 20 periods of the applied signal.[50] The Fourier spectrum of the applied signal, Figure 2b, shows that the applied signal only consists of the 3 kHz fundamental harmonic and has no higher order frequency components. This check ensures that any observed higher harmonic signal does not originate from the driving signal. The input signal-to-noise ratio (SNR) visible in Figure 2b is about 10^3.

The raw strain data in Figure 2c is noisy and subject to drift in the time domain. In the frequency domain, Figure 2d, the fundamental frequency of 3 kHz is clearly observed and no higher harmonics can be identified apart from some random noise peaks, which we attribute to numerical artefacts in the Fast Fourier Transform algorithm, since they have a very small peak width of only one frequency step. Below 2 kHz there is frequency dependent noise, which explains the drift in the time domain. The measured polarization signal, Figure 2e, has a constant amplitude of 1.35 μC cm^{-2}, but also drifts in time. Note that the amplitude of the polarization signal is small compared to the value of the remanent polarization, $P_r = 38.6$ μC cm^{-2}, as we only measure the change of the polarization. In the frequency domain, Figure 2f, one observes next to the fundamental frequency clearly higher harmonics, up to fifth order, superimposed on a decreasing frequency dependent noise baseline. The baseline was fitted with a linear function

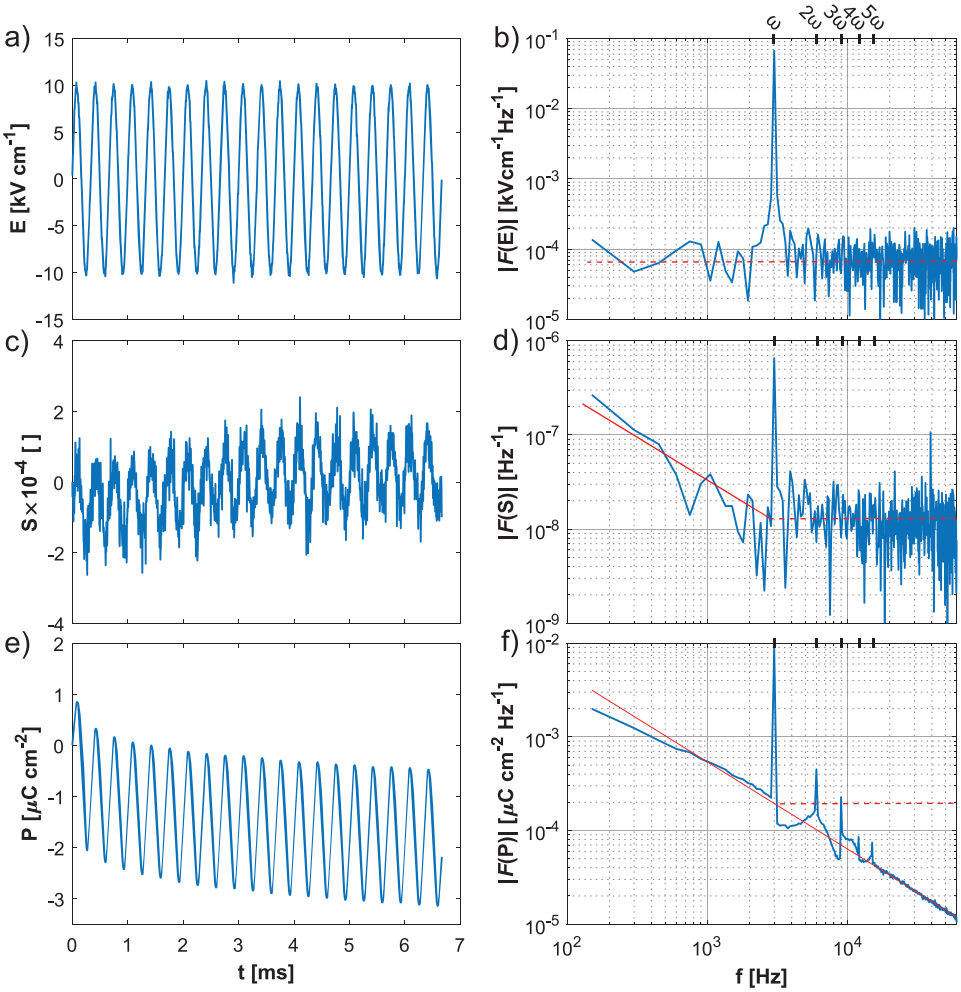

Figure 2. a, b) Applied electric field E, c, d) measured strain and e, f) polarization for an amplitude of 10 kV cm^{-1} and a frequency of 3 kHz in time (left) and frequency domains (right). Solid red line is the fitted 1/f noise and dashed red line is the noise baseline.

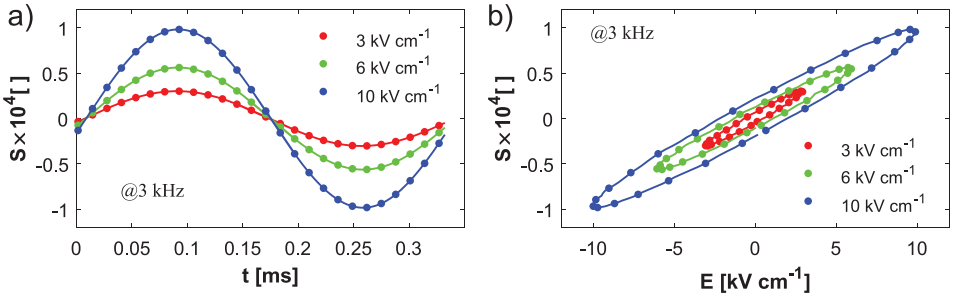

Figure 3. a) Filtered and averaged strain signal plotted with respect to time, and b) electric field, for three different field amplitudes at 3 kHz. Datapoints show the measurements and the lines are obtained from fitting with Equation (2).

in the log–log plot shown in Figure 2f, using the power-law dependence $P(f) = af^b$ with a and b being some fit parameters. For the complete data set, that is, for all amplitudes and frequencies, the exponent was obtained as $b = -0.92 \pm 0.03$, demonstrating the *1/f* character of the noise in the polarization measurements. The *1/f*-noise baseline extracted from the Fourier spectrum of the polarization signal, has been overlaid to the strain data in Figure 2d, showing a good match with the frequency dependent baseline in the strain. This observation suggests that the observed *1/f*-noise in both measurements has the same origin. The *1/f* dependence probably can tell something about the interaction mechanism of polarization and strain, but this is beyond the scope of this paper. The observed white noise in the strain at higher frequencies is not observed in the polarization and is thought to be linked to higher noise level in the displacement measurement method.

3.3. Strain Data

The drift, that is, low frequency noise in the strain data hinders an accurate fit of the model to the raw measurement data since the model predicts a purely sinusoidal strain signal. Therefore, the strain signal is filtered in the frequency domain by applying a bandpass filter around the fundamental harmonic. The filtered data is transformed back into the time domain and then averaged over the 20 measured cycles to increase the SNR. The averaged strain signal is plotted with markers with respect to time in **Figure 3**a and electric field in Figure 3b. The number of datapoints in one cycle was 128 but only every fifth datapoint is shown for clarity. The standard deviation of the averaged data was too small to be shown in the figure, as the associated error bars would be smaller than the datapoint markers. The hysteresis loops in Figure 3b are elliptical, in contrast to the lenticular loops, arising from the Rayleigh theory. The filtered and averaged strain data at 3 kHz in the time domain has been fitted with Equation (2) using the inverse of the standard deviations as the weighting factors and shown by the continuous lines in Figure 3a,b). The data and fits for all measured frequencies for 3 selected amplitudes are shown in Section 7, Supporting Information. The model fits the data points perfectly and all loops are traversed CCW, indicating that γ_d is negative, as is expected.

The extracted model parameters $d_{33,f}$ and γ_d are plotted versus E_0 in **Figure 4**a,b. The statistical uncertainty of individual model parameters is smaller than the datapoint markers and are therefore not shown. Both model parameters appear to fluctuate around an average value, independent of the field amplitude. To verify this observation, the average value and standard deviation σ (half of the red confidence intervals of the model parameters shown in Figure 4a,b) are propagated to the strain, resulting in a spread of 6%. This spread is below the 10% measurement-to-measurement accuracy of our strain measurements. This supports the conjecture that our model parameters are amplitude independent within the measurement accuracy of the used DBLI system. The average values of the fit parameters over the measured field range are $d_{33,f}$(3 kHz) = 96 pm V^{-1} and γ_d(3 kHz) = -9×10^{-11} cm kV^{-1} Hz^{-1} rad^{-1}. An independent measurement of the small signal piezoelectric constant at the same frequency measures $d_{33,f,ss}$ (3 kHz) = 93 pm V^{-1} as shown in Figure S5.1, Supporting Information, is in good agreement with the value extracted from the hysteresis measurements. Both values are in agreement with $d_{33,f}$ values of PZT films with similar stoichiometry, reported in literature.[28,51] In Figure 4c the loss tangent values for different excitation amplitudes, calculated from the hysteresis loop area, are shown with markers. In the same figure, the line denotes the average loss tangent calculated from Equation (3) using average values of $d_{33,f}$ (3 kHz) and γ_d (3 kHz). The confidence interval is obtained from the spread of values in these parameters. The loss tangent calculated from the area falls well within the confidence interval predicted by the model. Within measurement accuracy we can conclude that the strain loss tangent is independent of the amplitude, as was predicted by the model if $d_{33,f}$ and γ_d are independent of the excitation amplitude.

Figure 5a,b show the average values of $d_{33,f}$ and γ_d over the measured field range for different measurement frequencies and the error bars denote the standard deviation. Within the measurement range, the $d_{33,f}(f)$ data is practically frequency independent, so the weighted average and the corresponding confidence interval can be calculated. The field and frequency averaged value is $d_{33,f,av}$ = 98 pm V^{-1} that is denoted by the red line in Figure 5a. γ_d in Figure 5b does not show a frequency dependence if one neglects the low frequency data. The latter have large error bars originating from the dominant *1/f*-noise at these frequencies. The weighted average of all data points is $\gamma_{d,av} = -10 \times 10^{-11}$ cm kV^{-1} Hz^{-1} rad^{-1}. This value is very close to the high frequency data therefore we consider γ_d to be frequency independent over the whole measured frequency range. As both extracted parameters are amplitude and frequency independent, the viscosity constant

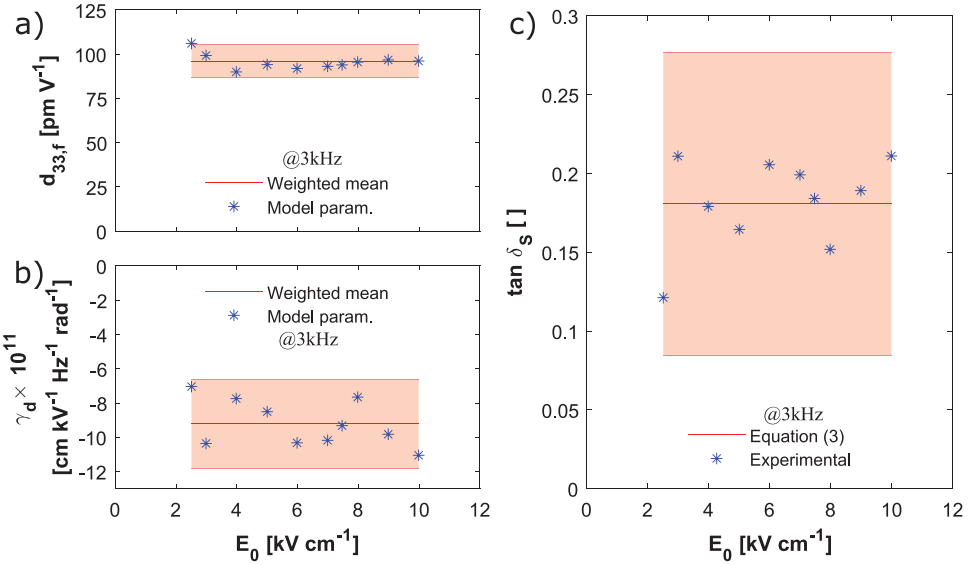

Figure 4. Field amplitude dependence of the extracted model parameters a) $d_{33,f}$, and b) γ_d. The red line denotes the weighted average of the model parameters, the red error corridor indicates the $\pm 2\sigma$ confidence intervals. c) tan δ_S calculated from the area of the *S-E* hysteresis loops. The red line and confidence interval are calculated with model Equation (3) using data from (a) and (b).

γ_S is $\gamma_{s,av} \approx -10 \times 10^{-6}$ Hz^{-1} rad^{-1}. Shown in Figure 5c is the loss tangent as function of frequency calculated from the area of the hysteresis loops using Equation S1.7, Supporting Information. The error bars again denote the standard deviation in the loop area for the measurements at different frequencies. The red line is calculated from Equation (3) with the average values $d_{33,f,av}$ and $\gamma_{d,av}$ and the error corridor is the corresponding $\pm 2\sigma$ confidence interval, due to error propagation of the confidence intervals of Figure 5a,b. The good linear scaling with frequency shows that the loss tangent is well described by Equation (3), supporting the validity of the viscous polarization rotation model. Further it indicates again that the parameters $d_{33,f}$, γ_d and resulting γ_S are independent of field amplitude and frequency. The Rayleigh model with viscous loss (see Section 1, Supporting Information) can explain the observed frequency dependency, but would predict a strong amplitude dependency of the loss tangent as in Equation S1.9, Supporting Information, which is absent in our measurement data.

To the best of our knowledge, in literature there is no experimental data for films of similar composition and the same amplitude and frequency, that would allow a direct comparison of the loss tangent with our results. However, the results

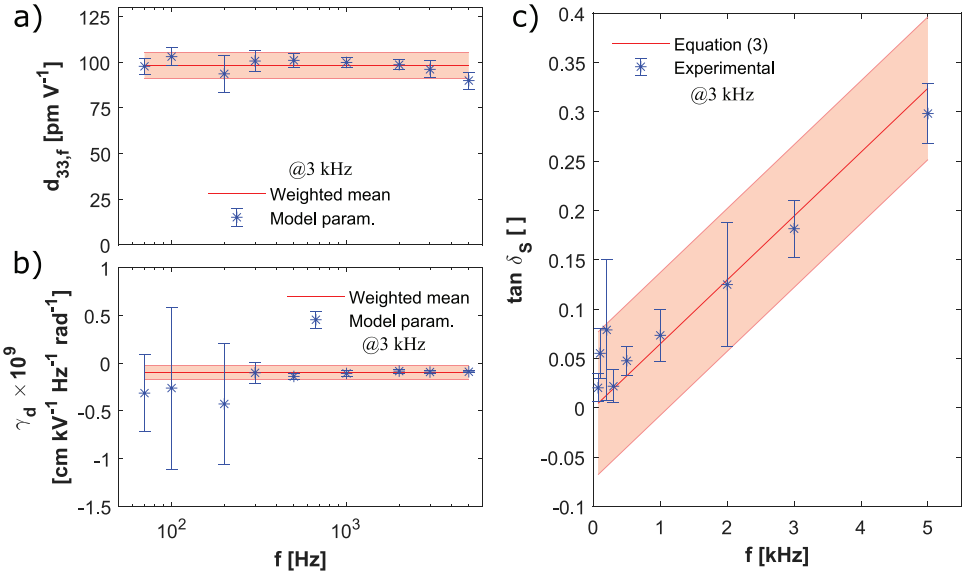

Figure 5. a) Averaged longitudinal piezoelectric coefficient $d_{33,f}$ and b) the viscosity parameter γ_d for all field amplitudes E_0. c) Loss tangent calculated from the area of the hysteresis loops. The red line is calculated with the field and frequency averaged values of $d_{33,f,av}$ and $\gamma_{S,av}$, using Equation (3). The error bars indicate the ±1 standard deviation of the data in all figures.

of Robert et al. allow a qualitative comparison.[42] They found a viscous loss tangent contribution of 0.044 ± 0.004, using the viscous Rayleigh model for the direct piezoelectric effect in a PZT ceramic (with composition near the morphotropic phase boundary) measured at 35 Hz. This value is comparable in magnitude to our value at 70 Hz of 0.020 ± 0.013. However, Robert et al. found this viscous term in addition to a dominant amplitude dependent Rayleigh term that increased up to 0.2 for the largest field amplitude. In our case such an amplitude dependent Rayleigh loss mechanism is not found. This difference is of interest since it indicates that the differences in loss behavior between our film and ceramics can be attributed to differences in crystal quality. Especially the number of defects in our epitaxial films is expected to be considerably smaller than in polycrystalline ceramics. Furthermore, the character of defects changes from dominantly lattice defects and vacancies for epitaxial films to grain boundaries in polycrystalline materials. This change in the character and the number of defects is expected to change the amplitude dependence of the loss. In polycrystalline materials the loss is dominated by the amplitude dependent part stemming from Barkhausen jumps of the pinned DWs in addition to the amplitude independent viscous part observed in both systems.[42]

3.4. Polarization Data

To extract the amplitude of the harmonics out of the polarization data, the peak value of the corresponding peak in the Fourier spectrum is taken. In **Figure 6**, the thus determined amplitudes $|P_i|$ of the 1st to 5th harmonic are shown as function of the field amplitude. The vertical scale for the 2nd to 5th harmonic is magnified for clarity. The solid lines correspond to the fits using the predicted dependencies on E_0 for the various harmonics according to Equation (8). The model is in very good agreement with the field dependence of the experimental data of the lower harmonics. The poorer fits for the 4th and 5th harmonic at low amplitudes are due to the low SNR for these harmonics. For Rayleigh behavior, the first harmonic is expected to scale as $P_1 \propto a_1 E_0 + a_2 E_o^2$ (with a_1 and a_2 some field independent constants), whereas in the polarization rotation model the dependence is of third order, $P_1 \approx P_{r,f}(k_{1,1}E_0 + k_{1,3}E_0^3)$.[37] Further, the Rayleigh model predicts that no even harmonics are present, which are clearly observed here. It predicts also that all other uneven harmonics scale with E_0^2, in contrast to $k_{n,n}E_0^n + k_{n,n+2}E_0^{n+2}$-scaling seen here. Although the first harmonic data might be fitted fairly well with the Rayleigh model, it is clear that the Rayleigh model completely fails to describe the field scaling of all other observed harmonics and the presence of the even harmonics.

As discussed, within the polarization rotation model the loss behavior can be approximated by the fundamental harmonic only. **Figure 7**a,b show the polarization hysteresis at selected amplitudes for 3 kHz. The data for all measured frequencies are shown in Section 8, Supporting Information. The data in these figures was obtained by bandpass filtering at all harmonic frequencies and then averaging over the measured 20 cycles. As for the strain the standard deviation calculated from the averaging is smaller than the marker size. Note that all higher

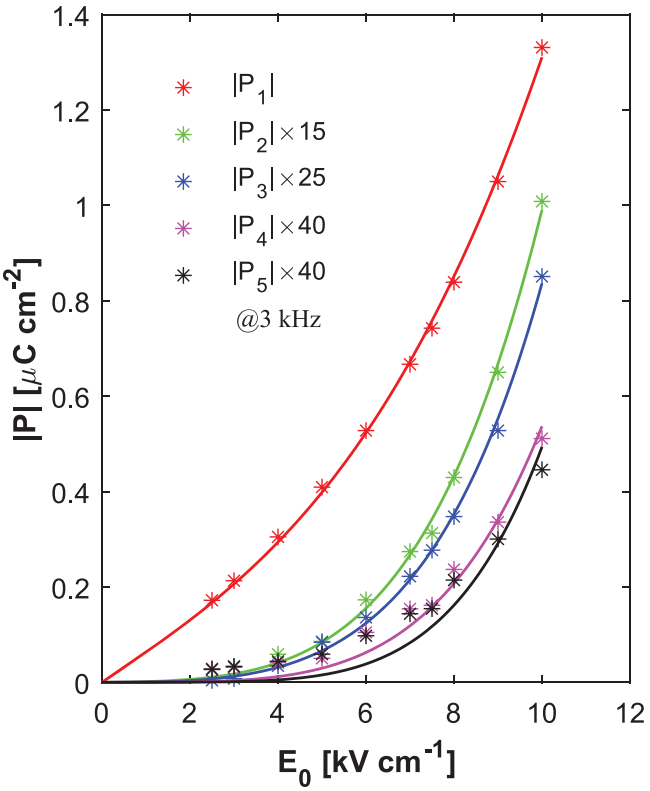

Figure 6. Scaling of the amplitude of the polarization harmonics with respect to the field amplitude E_0 at an excitation frequency of 3 kHz. The scaling of the 2nd to 5th harmonic is magnified for clarity. The data points are denoted by the stars and the lines are fits with Equation (8).

harmonics are included in these loops. The experimental loops were fitted with the fundamental harmonic only, using Equation (9) and taking into account the inherent phase shift present in the applied signal.[50] The good fits in time and field domain respectively show that, although the higher harmonics can be clearly observed in the frequency domain, their contributions are not visible in time or field domain except at the peaks of the 10 kV cm^{-1} amplitude measurement.

The loss tangent is proportional to the area of the *P-E* loop and inversely proportional to the polarization value at maximum field, therefore it can be concluded that the loss tangent calculated from the fundamental harmonic can accurately describe the field scaling of the loss. Figure 7c shows the amplitude dependence of the thus obtained loss tangent. The field dependence can be best fitted with a quadratic function with a constant offset of the form, $\tan\delta_P(E_0,\omega) = \tan\delta_P(0,\omega)(1+cE_0^2)$ with positive c, as shown by the red curve. The polarization rotation model in Equation (10) predicts no explicit field dependence for the loss tangent. The field dependence can only be implicit to the viscosity parameter with the same quadratic form $\gamma_P(E_0,\omega) = \gamma_P(0,\omega)(1+cE_0^2)$. From the loss tangent curve in Figure 7c at frequency $\omega_0 = 2\pi \times 3$ kHz one finds the model parameters, loss tangent at zero field as $\tan\delta_P(0,\omega_0) = 0.11$, c = 0.024 kV^{-2} cm^2, and thus $\gamma_P(0,\omega_0) = -5.84 \times 10^{-6}$ Hz^{-1} rad^{-1}. Interestingly $\gamma_P(0,\omega_0)$ is nearly equal in value to $\gamma_S(0,\omega_0)$, which is in-line with the expectation of Landau-Devonshire model that γ_P and γ_S should be identical. However, in contrast to γ_S being

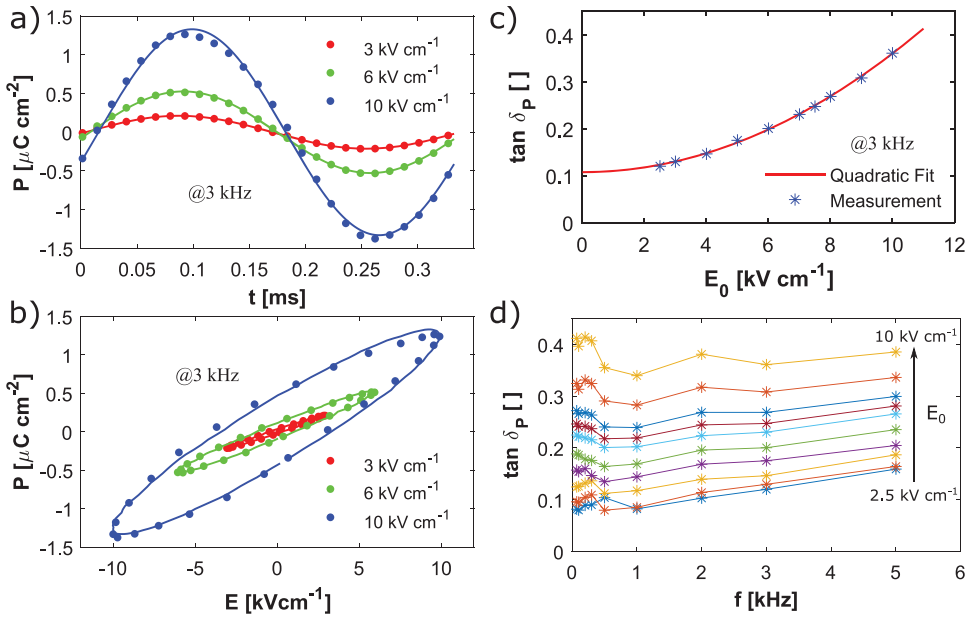

Figure 7. a) Filtered and averaged polarization signal plotted with respect to time, and b) electric field, for 3 different field amplitudes at 3 kHz. The markers represent the measured data, which includes all higher harmonics, and the solid lines are obtained by fitting with Equation (9). c) Loss tangent, calculated using Equation (10), is shown with markers. The red line denotes a fit with quadratic amplitude scaling as explained in detail in the main text. d) Frequency dependence of the loss tangent for all used amplitudes. Lines are guides for the eye connecting the data points.

field independent, γ_P shows a strong quadratic field dependence. We attribute the linearity of γ_S to the 4 orders of magnitude smaller relative change of strain compared to polarization.

The frequency dependencies of the loss tangent for all used field amplitudes are shown in Figure 7d. A linear increase is observed for frequencies above 500 Hz, which is typical for a viscous loss process and is as described by the proposed polarization rotation model. The deviation for lower frequencies may be explained by the fact that for these frequencies the coercive field is lower, so that the field is swept up to $¾E_c$ or even higher as can be seen in Table S6.1, Supporting Information. The nonlinearity is then larger, which changes the values of the β-parameters and thus of the loss. The observed amplitude and frequency dependency of the loss tangent for the polarization deviates clearly from the predicted dependencies of the Rayleigh model, as it is also the case for the strain.

4. Conclusions

In summary, we observe experimentally a linear hysteretic strain behavior and nonlinear hysteretic polarization behavior for an epitaxial PZT film with monoclinic symmetry. The nonlinearity is characterized by the presence of all even and odd order harmonics observable up to 5th order in the polarization measurements. These findings are explained by a model that relates the rotation of the polarization vector in the (110)-plane of a pseudocubic unit cell in response to an applied electric field, as is expected for the used PZT film with monoclinic symmetry. The polarization rotation is accompanied by viscous interactions for the strain and polarization response of the film. The strain behavior is described by a linear field dependent stretching of the unit-cell due to the rotation of the polarization vector. This strain model describes in detail the field amplitude and frequency dependence of the measured strain and loss tangent. The polarization is described by the rotation of the polarization vector, which has a nonlinear dependence on the field, and a viscous interaction. The model predicts all of the observed even and odd harmonics and their amplitude scaling. The polarization rotation model takes into account the crystal symmetry of the unit cell, in contrast to the Rayleigh model, hence is expected to be applicable to other material systems in which polarization rotation is present, such as in monoclinic, rhombohedral or similar crystal symmetries.

5. Experimental Section

Film Deposition: The PZT film near the MPB with tetragonally distorted rhombohedral or monoclinic crystal symmetry was grown by PLD with a KrF excimer laser source (Lambda Physic, 248 nm wavelength). The target and film composition were determined by X-ray fluorescence and Rutherford Back Scattering (RBS) to be $PbZr_{0.55}Ti_{0.45}O_3$ (Kurt J. Lesker), hence in the rhombohedral range of the PZT phase diagram. The PZT film was sandwiched between two 100 nm thick LNO electrodes, also deposited by PLD, on a STO substrate. The PZT thickness was about 3 µm, calculated from the deposition rate and deposition time. The LNO electrodes were deposited with a laser repetition rate of 4 Hz, energy density of 2.25 J cm^{-2}, laser spot size of 3 mm^2, target-to-substrate distance of 60 mm, oxygen pressure of 0.1 mbar, and a substrate temperature of 600 °C. The PZT film was deposited with a laser repetition rate of 10 Hz, energy density of 2 J cm^{-2}, laser spot size of 3 mm^2, target-to-substrate distance of 55 mm, 0.1 mbar O_2, and at 600 °C. The layers were deposited successively without breaking the vacuum. After deposition, the film was cooled down to room temperature in 1 bar O_2 atmosphere at a cooling rate of 8 °C min^{-1}. For ferro/piezoelectric measurements a 100 nm thick platinum (Pt) layer was deposited on top by sputtering, from which 300 × 300 $µm^2$

top electrodes of the capacitors were patterned with a standard photolithography process and structured by argon ion beam etching of the top Pt and LNO layers. The bottom electrode is contacted by use of silver glue at the side of the sample.

Analysis and Characterization: Crystallographic properties of the PZT film were analyzed by a X-ray diffractometer (Bruker D8 Discover) equipped with a high brilliance microfocus Cu rotating anode generator, Montel optics, a Ge (220) two-bounce monochromator, a double pinhole beam collimator with a diameter of 200 µm, and an area detector (EIGER2 R 500K). The asymmetric reciprocal space maps were reconstructed from sets of high-resolution rocking curves. All XRD measurements shown in this work were performed on a single, unpoled capacitor.

The piezoelectric and ferroelectric properties were measured with a double beam laser interferometer (aixDBLI), to eliminate the influence of substrate bending, utilizing a ferroelectric tester (aixACCT TF-2000 Analyzer) to measure the ferroelectric properties. The large field polarization and strain (global *P-E* and *S-E*, respectively) loop measurements were performed using a sinusoidal AC-electric field with an amplitude of 200 kV cm^{-1} at 3 kHz. The coercive field of the film was around 24 kV cm^{-1}. The small signal $d_{33,f}$ measurements were carried out using a lock-in technique with a DC-driving field in the range of 200 kV cm^{-1} and an AC peak-to-peak amplitude of 1.6 kV cm^{-1} at a frequency of 3 kHz.

The sub-coercive field hysteresis behavior was measured using 20 cycles of sinusoidal signal with peak-to-peak amplitude ranging from 2.5 to 10 kV cm^{-1}. The measurement frequency was varied from 70 Hz to 5 kHz. Before each sub-coercive field measurement the film was poled with a DC field of 200 kV cm^{-1}, to realize comparable starting conditions. The sub-coercive field polarization and strain responses were measured simultaneously, at room temperature and with zero bias fields.

Supporting Information

Supporting Information is available from the Wiley Online Library or from the author.

Acknowledgements

This work is part of the research programme "Smart Multilayer Interactive Optics for Lithography at Extreme UV wavelengths (SMILE)", with contract number 10448 and financial support by the Nederlandse Organisatie voor Wetenschappelijk Onderzoek (NWO) and Carl Zeiss SMT. This research has been carried out in Industrial Focus Group XUV Optics and Inorganic Material Science Group at the MESA+ Institute for Nanotechnology of the University of Twente. Industrial Focus Group XUV Optics receives further support by the Province of Overijssel, ASML and Malvern Panalytical. The RBS measurements were performed by Dr. Max Doebeli of the Ion Beam Physics group of the ETH Zurich, Switzerland.

Conflict of Interest

The authors declare no conflict of interest.

Keywords

ferroelectrics, hysteresis, nonlinearity, piezoelectric

Received: June 26, 2020
Revised: September 8, 2020
Published online: September 23, 2020

[1] R. Waser, *Adv. Mat.* **1992**, *4*, 311.
[2] N. Setter, D. Damjanovic, L. Eng, G. Fox, S. Gevorgian, S. Hong, A. Kingon, H. Kohlstedt, N. Y. Park, G. B. Stephenson, I. Stolitchnov, A. K. Taganstev, D. V. Taylor, T. Yamada, S. Streiffer, *J. Appl. Phys.* **2006**, *100*, 051606.
[3] P. Muralt, *J. Am. Ceram. Soc.* **2008**, *91*, 1385.
[4] P. Muralt, R. G. Polcawich, S. Trolier-McKinstry, *MRS Bull.* **2009**, *34*, 658.
[5] C.-B. Eom, S. Trolier-McKinstry, *MRS Bull.* **2012**, *37*, 1007.
[6] M. Bayraktar, A. Chopra, G. Rijnders, K. Boller, F. Bijkerk, *Opt. Express* **2014**, *22*, 30623.
[7] M. Nematollahi, P. Lucke, M. Bayraktar, A. Yakshin, G. Rijnders, F. Bijkerk, *Opt. Lett.* **2019**, *44*, 5104.
[8] M. Bayraktar, W. A. Wessels, C. J. Lee, F. A. van Goor, G. Koster, G. Rijnders, F. Bijkerk, *J. Phys. D: Appl. Phys.* **2012**, *45*, 494001.
[9] B. Jaffe, W. R. Cook, H. Jaffe, in *Piezoelectric Ceramics*, https://doi.org/10.1016/B978-0-12-379550-2.50011-9 (Eds: B. Jaffe, W. R. Cook, H. Jaffe), Academic Press, New York **1971**, p. 135.
[10] P. Muralt, *J. Micromech. Microeng.* **2000**, *10*, 136.
[11] S. Trolier-McKinstry, P. Muralt, *J. Electroceram.* **2004**, *12*, 7.
[12] H. Yang, F. Yan, Y. Lin, T. Wang, *ACS Sustainable Chem. Eng.* **2017**, *5*, 10215.
[13] J. O. Gentner, P. Gerthsen, N. A. Schmidt, R. E. Send, *J. Appl. Phys.* **1978**, *49*, 4485.
[14] B. Laikhtman, *Phys. Solid State* **1973**, *15*, 62.
[15] V. Postnikov, V. Pavlov, S. Gridnev, S. Turkov, *Phys. Solid State* **1968**, *10*, 1267.
[16] V. Postnikov, V. Pavlov, S. Gridnev, B. Darinskii, I. Glozman, *Bull. Russ. Acad. Sci.: Phys.* **1967**, *31*, 1888.
[17] G. Arlt, H. Dederichs, *Ferroelectrics* **1980**, *29*, 47.
[18] L. Rayleigh, *London Edinburgh Dublin Philos. Mag. J. Sci.* **1887**, *23*, 225.
[19] L. Néel, *Cah. Phys.* **1942**, *12*, 1.
[20] L. Néel, *Cah. Phys.* **1943**, *13*, 18.
[21] D. Damjanovic, M. Demartin, *J. Phys. D: Appl. Phys.* **1996**, *29*, 2057.
[22] G. Bertotti, V. Basso, G. Durin, *J. Appl. Phys.* **1996**, *79*, 5764.
[23] G. Bertotti, *Phys. Rev. Lett.* **1996**, *76*, 1739.
[24] D. A. Hall, *J. Mater. Sci.* **2001**, *36*, 4575.
[25] D. V. Taylor, D. Damjanovic, *J. Appl. Phys.* **1997**, *82*, 1973.
[26] D. Damjanovic, *Phys. Rev. B: Condens. Matter Mater. Phys.* **1997**, *55*, R649.
[27] D. Damjanovic, S. S. N. Bharadwaja, N. Setter, *Mater. Sci. Eng., B* **2005**, *120*, 170.
[28] K. Vergeer, *PhD Thesis*, Universiteit Twente, Enschede, the Netherlands **2017**.
[29] F. Preisach, *Z. Phys.* **1935**, *94*, 277.
[30] G. Robert, D. Damjanovic, N. Setter, *J. Appl. Phys.* **2001**, *90*, 2459.
[31] G. Robert, D. Damjanovic, N. Setter, A. Turik, *J. Appl. Phys.* **2001**, *89*, 5067.
[32] D. Damjanovic, in *The Science of Hysteresis*, https://doi.org/10.1016/B978-012480874-4/50022-1 (Eds: G. Bertotti, I. D. Mayergoyz), Academic Press, Oxford **2006**, Ch. 4, p. 337.
[33] D. V. Taylor, D. Damjanovic, *Appl. Phys. Lett.* **2000**, *76*, 1615.
[34] A. Pramanick, D. Damjanovic, J. C. Nino, J. L. Jones, *J. Am. Ceram. Soc.* **2009**, *92*, 2291.
[35] D. V. Taylor, D. Damjanovic, N. Setter, *Ferroelectrics* **1999**, *224*, 299.
[36] D. V. Taylor, D. Damjanovic, E. Colla, N. Setter, *Ferroelectrics* **1999**, *225*, 91.
[37] D. Damjanovic, D. V. Taylor, *Ferroelectrics* **1999**, *221*, 137.
[38] N. Bassiri-Gharb, I. Fujii, E. Hong, S. Trolier-Mckinstry, D. V. Taylor, D. Damjanovic, *J. Electroceram.* **2007**, *19*, 47.
[39] N. Bassiri-Gharb, S. Trolier-McKinstry, D. Damjanovic, *J. Appl. Phys.* **2011**, *110*, 124104.
[40] N. B. Gharb, S. Trolier-McKinstry, D. Damjanovic, *J. Appl. Phys.* **2006**, *100*, 044107.

[41] S. Trolier-McKinstry, N. Bassiri Gharb, D. Damjanovic, *Appl. Phys. Lett.* **2006**, *88*, 202901.
[42] G. Robert, D. Damjanovic, N. Setter, *J. Appl. Phys.* **2001**, *90*, 4668.
[43] M. J. Haun, E. Furman, S. J. Jang, L. E. Cross, *Ferroelectrics* **1989**, *99*, 63.
[44] In ref. [45 46] it was shown, by Landau-Devonshire modelling of a clamped rhombohedral film on STO with PZT60/40 composition, that the contribution to polarization change due to polarization rotation is a factor 3.2 larger than for polarization extension.
[45] E. P. Houwman, K. Vergeer, G. Koster, G. Rijnders, in *Correlated Functional Oxides*, Springer, Berlin **2017**, Ch. 2, p. 29.
[46] E. Houwman, K. Vergeer, G. Koster, G. Rijnders arXiv:1901.10883 **2019**.
[47] In principle θ(E) can be calculated from a Landau-Devonshire description for a clamped film. In [45 46] this was done from a numerical evaluation of a Landau-Devonshire-model for $E = 0$ and 200 kVcm-1. However, since it is difficult to take into account the deformation of the unit cells in a polydomain film, we will here use the above phenomenological description and use the experimental fit parameters to describe (E).
[48] B. Noheda, D. E. Cox, G. Shirane, R. Guo, B. Jones, L. E. Cross, *Phys. Rev. B: Condens. Matter Mater. Phys.* **2000**, *63*, 014103.
[49] M. D. Nguyen, M. Dekkers, E. Houwman, R. Steenwelle, X. Wan, A. Roelofs, T. Schmitz-Kempen, G. Rijnders, *Appl. Phys. Lett.* **2011**, *99*, 252904.
[50] The applied signal does not always start at 0 for t = 0 as assumed in the model. To compare the results with the model, we fit the applied signal with a phase shift sine wave for each measurement to extract the initial phase shift Φ, that is in the range $\pm 3°$ for the used amplitudes and frequencies. This additional step is needed to exclude any non-material induced phase change.
[51] R. J. A. Steenwelle, *PhD Thesis*, Universiteit Twente, Ipskamp Printing, Enschede **2012**.